Distributed Intelligent Energy Management System for a Single-Phase High-Frequency AC Microgrid

Sudipta Chakraborty, *Student Member, IEEE*, Manoja D. Weiss, *Member, IEEE*, and M. Godoy Simões, *Senior Member, IEEE*

***Abstract*—In this paper, a single-phase high-frequency AC (HFAC) microgrid is shown as a novel solution towards integrating renewable energy sources in a distributed generation system. Better utilization of the Microgrid is achieved by solving power flow and power quality issues using p-q theory-based active filtering called universal active power line conditioner and unified power quality conditioner, respectively. A distributed intelligent energy management system (DIEMS) is implemented to optimize operating costs. As the optimization greatly depends on the power generation and the power output from renewable sources strongly depends on the weather, the forecast of power generation is required for DIEMS. A Fuzzy ARTMAP neural network is used to predict hourly day-type outputs based on which generation can be forecasted. Depending on the forecast, an optimization scheme is developed utilizing linear programming along with heuristics. The results obtained show the successful implementation of HFAC Microgrid with adequate power flow and power quality control, as well as the optimization of operation cost by the DIEMS with Fuzzy ARTMAP-based day-type forecasting. The improvement in the battery life is also achieved due to optimization of storage charge states using the proposed DIEMS.**

***Index Terms*—Active filters, distributed intelligent energy management system (DIEMS), fuzzy ARTMAP, high-frequency AC (HFAC), linear programming, microgrid, unified power quality conditioner (UPQC), universal active power line conditioner (UPLC).**

I. Introduction

MICROGRID is a relatively new concept in the electric power distribution. In a Microgrid, a cluster of loads and microsources operate as a single controllable system to provide power and heat in their local area [1]. The capability of adding a number of smaller generation technologies, such as wind, hydro, photovoltaic (PV), fuel cells, gas turbines, batteries, ultra-capacitors, and flywheels, makes the Microgrid a very promising option for on-site power generation by the end-users. In the modern power scenario where deregulation and state policies encourage end-users to generate their own power in forms of distributed generation (DG) [2], the Microgrid concept is a big step towards solving the controllability problems of distributed resources.

Power electronic converters are very important for the Microgrid. The majority of microsources must be power electronic based to provide required flexibility to insure operation as a single aggregated system. In the proposed structure, a high-frequency AC (HFAC) link has been used as the power electronic interface to achieve better utilization of the Microgrid. Single-phase 500 Hz high-frequency buses are used to combine the renewable sources with the loads and the grid. The advantages and considerations of HFAC system will be addressed in this paper along with the possible applications of the 500 Hz system. In the HFAC Microgrid, voltage distortions are present due to source and/or converter nonlinearity along with the load current harmonics resulted from nonlinear loads, which cause power quality control an important issue. The proposed system utilizes an active filter called unified power quality conditioner (UPQC) to compensate for these voltage and current harmonics [3], [4]. The control of active and reactive power flow between the microsources and the grid is also very important for proper utilization of the Microgrid. A universal active power line conditioner (UPLC) [4], [5] is used to control the power flow from/to Microgrid. Though the UPQC and UPLC have the same basic blocks, known as shunt and series active filters, the controls for both of them as well their functionalities are different. In the UPQC, both the shunt and series active filters are used for harmonics mitigation, so it can be considered as the complete filtering solution. On the other hand, the main function of the series active filter in UPLC is to control the active and reactive power flow. The change in control algorithm of the series active filter, therefore, enables UPLC to work as a combination of UPQC and active power flow controller. Both UPQC and UPLC consist of series and shunt active filters that use instantaneous power theory (p-q theory) [6] to calculate compensating voltage and currents. The compensating voltage and currents are then synthesized using voltage-source pulsewidth modulation (PWM) inverters [4].

After the structure of the HFAC Microgrid is defined, the optimization of the operating cost is the next challenge. A distributed intelligent energy management system (DIEMS) has been implemented for cost optimization. The function of the system is to generate set points for all the sources and storages in such a way that economically optimized power dispatch will be maintained to fulfill certain load demand. The DIEMS consists of two levels of operations. The optimization level needs the forecasts of generations with considerable accuracy by a prediction level. The forecast of generation is a challenging task for the Microgrid system as the sources connected are mainly the renewable energy sources where the capacity of generation varies largely with the external conditions like sunshine, temperature, etc. [7].

To avoid complexities of mathematical model-based statistical prediction, a neural network (NN) is incorporated in

Manuscript received October 24, 2005; revised March 2, 2006. Abstract published on the Internet November 30, 2006. This work was supported in part by the National Science Foundation (NSF).

The authors are with the Colorado School of Mines, Golden, CO 80401 USA (e-mail: schakrab@mines.edu; mweiss@mines.edu; msimoes@mines.edu).

Digital Object Identifier 10.1109/TIE.2006.888766

DIEMS. NNs are a very efficient and capable tool for this type of nonlinear mapping. But unfortunately, the simple backpropagation-based NN cannot be used for weather forecasting because such network overwrites previously trained information when presented with new information that does not fit learned patterns. What is needed for this application is a network that selectively learns novel patterns when it cannot find an appropriate match with existing patterns. This "stability-plasticity dilemma" was addressed directly by the adaptive resonance theory (ART) NNs developed by Grossberg and Carpenter of Boston University [8]–[12]. Out of several ART structures, Fuzzy ARTMAP is used in the proposed system for forecasting power generation. Fuzzy ARTMAP is a class of ART NN architecture that performs incremental supervised learning of recognition categories and multidimensional maps in response to input vectors presented in arbitrary order [11]. This NN has the ability to learn novel information without forgetting the previously trained information. It learns to classify inputs by a fuzzy set of features, or a pattern of fuzzy membership values indicating the extent to which each feature is present. The prediction module in DIEMS requires hourly metrological information (solar radiation, temperature, pressure, relative humidity) and time information as inputs. The system output is the hourly day-type forecast which is used to determine and continuously refine a specific set of operating conditions for cost optimization.

Based on the output of the forecasting module, that is the day-type of present day and the next day, the DIEMS optimization module chooses one of the predesigned optimization schemes such that the cost of operation is minimized. In each of these optimization schemes, linear programming is used along with some heuristics. The information of the next hour day-type is also utilized to define the threshold for charging and discharging rate for a particular hour. Linear programming is then used for optimization of operating cost. In each optimization steps, the power balance and storage states are considered to obey the physical constraints. The output of this module defines the power flow direction and amount of flow between sources, storages, loads and grid in a cost optimized way.

Section II of this paper describes the advantages of the HFAC system along with the considerations in choosing the suitable frequency of operation. The possible applications of the 500 Hz high-frequency system is also discussed in this section. The following section covers, in brief, the operation of the single-phase HFAC Microgrid system with UPLC and UPQC. The interaction between the HFAC Microgrid and supervisor level DIEMS controller is discussed in Section IV. Also, given in this section, the details about the Fuzzy ARTMAP forecasting module and linear programming-based optimization module. The simulation results justifying the claims of power flow and power quality control are shown in Section V along with the results of cost optimization by DIEMS. Finally, this paper is concluded in Section VI with some pertinent remarks.

II. HFAC Systems: Advantages and Considerations

The series resonant converters, utilizing zero-voltage or zero-current switching, can be used with each of the sources to generate the HFAC link. In this way, the overall losses in the converters can be reduced [13].

A. HFAC Advantages

A HFAC system will have the following inherent advantages, as discussed in [4] and [14].

- The harmonics are of higher orders and easily filtered out.
- Fluorescent lighting will experience improvement as with higher frequency the luminous efficiency is improved, flicker is reduced, and dimming is accomplished directly. The ballast inductance is reduced proportionally to the frequency with the corresponding reduction in the size and weight.
- High-frequency induction motors can be used for compressors, high-pressure pumps, and turbines. AC frequency changers based on matrix converters can be used to soft-start high-frequency induction motors.
- Harmonic ripple current in electric machines will decrease, improving efficiency.
- High-frequency power transformers and other passive circuit components become smaller.
- The size of harmonic filters for batteries will decrease.
- Auxiliary power supply units are easily available by tapping the AC link. They would be smaller with better efficiencies.
- Storage units are required for Microgrid to improve reliability. Batteries have been the traditional energy storage source, but in HFAC Microgrid dynamic storage such as flywheel is also an easy alternative.

B. Power Transmission and Distribution at High Frequencies

Two significant factors that affect the suitability of power transmission and distribution at high frequencies are the increased power losses and voltage drop incurred along the line. The power losses cause heating and system inefficiency, while the voltage drop results in the voltage delivered to the load at lower level. Both these factors increase with line length and frequency, and therefore impose a frequency-dependent limitation on the size of a useful high-frequency grid. To properly examine this limitation, it is necessary to begin with the type of cable that will be used and create a frequency-dependent circuit model of its defining parameters. In the following, an analysis using simple single-core coaxial cable with a grounded sheath will be used for demonstration purposes. It is possible to extend this analysis to any type of cable, provided its geometry and frequency-dependent material properties are known.

C. Cable Circuit Model

The cross section of a coaxial transmission cable with a single core and grounded sheath is shown in Fig. 1(a), and its small segment circuit model is shown in Fig. 1(b). To satisfy the assumption of small electrical size, the total length of this transmission line segment must be less than about 1/10 of the wavelength. At 60 Hz, 1/10 of a wavelength is 500 Km, whereas at 500 Hz, this would be about 60 Km. For cables longer than 1/10 of a wavelength, more sections must be used to model the line correctly and for electrically long lines, a distributed circuit model is used [15]. It is assumed that the guided energy is in the form of a

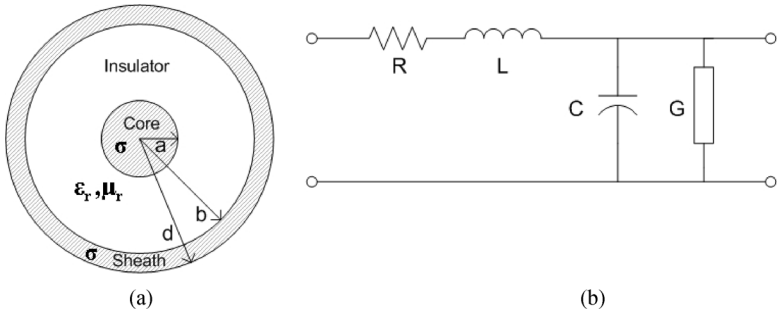

(a) (b)

Fig. 1. Small segment of insulated, grounded electrical cable. (a) Cross section. (b) Circuit model.

transverse electromagnetic field where the fields are perpendicular to the direction of propagation. The frequency-dependent parameters of this small section are the series impedance $Z(\omega)$ consisting of a resistance $R(\omega)$ and an inductance $L(\omega)$, and a shunt admittance $Y(\omega)$ composed of a capacitance $C(\omega)$ and a conductance $G(\omega)$. For a multiple conductor transmission line, $Z(\omega)$ and $Y(\omega)$ are square matrices, with self and mutual coupling terms [16]

$$Z(\omega) = R(\omega) + j\omega L(\omega) \tag{1}$$
$$Y(\omega) = G(\omega) + j\omega C(\omega). \tag{2}$$

$Z(\omega)$ and $Y(\omega)$ are found through electromagnetic analysis and simulation, given the geometry and the material properties: relative permittivity (ε_r), relative permeability (μ_r), and conductivity (σ). This process was demonstrated for two specific types of transmission lines in [17]. $R(\omega)$ and $G(\omega)$ represent losses, whereas the series inductance $L(\omega)$ gives rise to a large voltage drop along the line. The self-inductance is neglected as it is very small compared to the mutual inductance between the core and the sheath.

D. Power Loss Along the Line

As stated earlier, the transmission of power along cables is subject to losses that are frequency-dependent. Among these high-frequency loss mechanisms are the skin effect in the center conductors, dielectric relaxation in the insulators, eddy currents in any metal enclosures, and the proximity effect. Loss due to the dielectric insulating material is represented by a shunt conductance, and is caused by currents that leak between the two conductors through the dielectric. For most of the cables, especially those using XLPE or PE as an insulator, dielectric loss does not play a big role in the attenuation of power below about 1 MHz and eddy current losses can be neglected below about 100 kHz [18].

The dominant cause of power loss at frequencies below 10 kHz is the skin effect [18]. It is characterized by the skin depth, which is a figure of merit for the depth of penetration of the electric field into the conductor. The skin depth is related to the frequency as given below

$$\delta_c = \frac{1}{\sqrt{\pi f \mu_0 \sigma}} \tag{3}$$

where μ_0 is the free-space permeability, f is the frequency of operation, and σ is the conductivity of the metal conductor.

For AC signals, the series resistance is determined as follows:

$$R_{\mathrm{AC}} = R_{\mathrm{in}} + R_{\mathrm{out}} \tag{4}$$
$$R_{\mathrm{in}} = \frac{1}{(2\pi\sigma\delta_c^2)\left(\frac{a}{\delta_c} - 1 + e^{-a/\delta_c}\right)} \tag{5}$$
$$R_{\mathrm{out}} = \frac{1}{(2\pi\sigma\delta_c^2)\left(\left(\frac{b}{\delta_c}+1\right) - \left(\frac{d}{\delta_c}+1\right)e^{(b-d)/\delta_c}\right)} \tag{6}$$

where a is the conductor radius, b is the inner radius of the sheath, and d is the outer radius of the sheath, as shown in Fig. 1(a).

At low frequencies, if the conductor thickness is much less than the skin depth, there is an approximately uniform current density on the conductor, and therefore the series resistance is the same as the DC series resistance. At frequencies where the skin depth is comparable to or less than the conductor thickness, the series resistance is higher than the DC value since the current is forced through a smaller cross section than the physical area available.

The attenuation α of the line, in dB/m is given by

$$\alpha = 8.68\left(\frac{R + GZ_0^2}{2Z_0}\right) \tag{7}$$
$$Z_0 = \sqrt{\frac{L}{C}}. \tag{8}$$

The above formula for α has assumed that the cable is a low-loss cable ($R \ll j\omega L$ and $G \ll j\omega C$). Even though this is not strictly true at low frequencies since ω is very small, the general trends of the graph at frequencies below 500 Hz are qualitatively applicable.

Fig. 2 shows the cable attenuation as a function of frequency for a single-core grounded-sheath coaxial cable with a copper core and sheath and an insulating layer between the two conductors with permittivity given by the following Debye model [16]. The parameters used for Fig. 2 are $a = 1$ mm, $b = 6$ mm, $d = 6.2$ mm, $\mu_r = 1$, $\sigma = 5.8 * 10^{-7}$ S/m, and $\varepsilon_r = 2.5 + 0.94/(1 + j\omega 6 * 10^{-9})^{0.315}$. The attenuation at 500 Hz is about $2\mathrm{e}-4$ dB/m, or 0.2 dB/km. This will determine the size of the grid, depending on the tolerable losses.

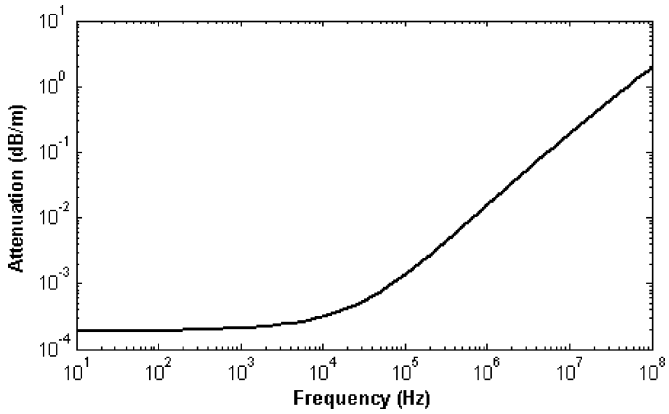

Fig. 2. Frequency dependence of cable attenuation.

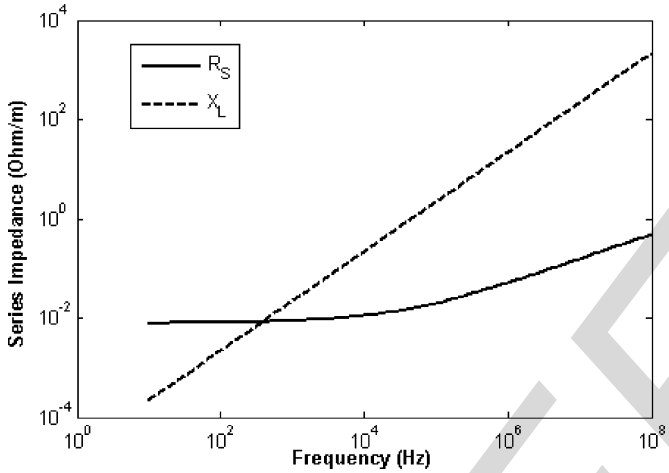

Fig. 3. Frequency dependence of series impedance.

E. Voltage Drop

The voltage drop along the line is due to the series impedance $Z(\omega)$. As can be seen in Fig. 3, at frequencies below about 500 Hz, this voltage drop is mainly due to the series resistance $Re(Z)$. Above this frequency, the series impedance, represented by the reactance $\mathrm{Im}(Z) = j\omega L$, dominates the voltage drop. Fig. 3 can be used to calculate the voltage drop in volts if the line current and the length of the line are known. The allowable voltage regulation is around 5% in the U.S., which at 330 V level gives the allowable voltage drop of 16.5 V. From Fig. 3, the series impedance at 500 Hz is approximately $0.01 + \mathrm{j}0.01\ \Omega/\mathrm{m}$. That gives the maximum length of the cable at 7 A, 500 Hz as 235 m. The current is decided based on the loads in the load bus of the simulations, as shown in the following results section. So, there is no need of voltage restorer if the Microgrid system supplies power within a radial area of 235 m. The voltage compensation techniques for the higher frequencies are an active field of research [19] and not in the scope of this work, but for the Microgrid system proposed here, small voltage drops can be compensated by the active filters already in the system [5]. With a lower distribution level such as three-phase 6 KV, it is possible to supply power within a 1-by-1 Km commercial zone using the conventional three-phase cable [20].

F. Applications of 500 Hz HFAC

The use of 400 Hz power sources is widespread in the military and aircraft industries to reduce the component size and weight. Due to several physical limitations, such as increased power loss and voltage drop, of going towards very high-frequency, it had been shown that the frequency in the range of 400 Hz to 1 KHz is suitable for several residential, industrial, and commercial applications [20], [21]. Some of those applications for a 500 Hz power system are given below [20].

- High-speed motors having capacity up to 25 MW and speed of 5000 rpm are used in the turbine compressors for condensation of gases, as well as for blowers. In the 500 Hz system, the low cost, highly reliable induction motors are the better option for those applications.
- In the iron and steel industry, 400 Hz to 1 KHz power is very useful for melting in induction furnace and for heat treatment due to the high-efficiency, compact equipments, and ease of control. Besides, the size of the capacitor required for power factor improvement will also be less at 500 Hz frequency compared with that at 60 Hz.
- The commercial loads mainly constitutes of lighting and air conditioning. At 500 Hz, though there will not be significant improvement of the luminous efficiency, the amorphous core ballasts can be used to increase the overall efficiency. Additionally, the size of the lighting apparatus will be reduced to 500 Hz, improving the space savings in commercial buildings.
- The same benefits as above can be utilized for the residential buildings. With the integration of renewable sources into the system, such benefits will provide additional advantages when supplying power to isolated locations without strong grid support.
- Quick response dc power supply using simpler control such as deadbeat control can be used more easily with 500 Hz.

III. Single-Phase HFAC Microgrid With Active Filters

The right-hand side of Fig. 4 depicts the single-phase HFAC-based Microgrid along with the UPQC and UPLC. There are four high-frequency buses in the Microgrid system as described next.

In the source bus (or Bus 1), a variety of renewable sources are connected along with energy storage systems (battery). The utility grid is connected in utility connection bus (or Bus 2) through a bidirectional converter and associated loads. In load bus (or Bus 3), high-frequency loads are connected. The intermediate supply bus gets its supplies from Bus 1 and Bus 2. It then sends the power to Bus 3 (load bus).

The integration of the single-phase high-frequency AC Microgrid with the three-phase 60 Hz utility grid can be achieved by using frequency link converters such as PWM-controlled dc link back-to-back converter or matrix converter without a dc link. The main characteristics for those converters are the bidirectional power flow capability which is required for the proposed system. The 60 Hz loads can be connected to the load bus using the similar converters. Another effective way for connecting 60 Hz loads to the Microgrid is to use naturally commutated cycloconverters. The higher frequency of the HFAC system is useful for such cycloconverters as the output

frequency limitation is no longer an issue, and it can generate the 60 Hz output frequency [20]. In this paper, the high-frequency loads are only considered in simulations which represent the loads that can be connected directly to the 500 Hz HFAC Microgrid based on the possible applications, as discussed in the previous section.

Bus 1 and Bus 2 are connected by a controlled distribution line through a UPLC. The main function of the UPLC is to control the power flow between the source bus and the utility connection bus. The UPLC also mitigates current harmonics present in the utility connection bus due to the connection of the bidirectional converter.

To maintain the power balance of the whole system with UPLC, another uncontrolled distribution line is required. In the Microgrid, the intermediate supply bus, connected to both Bus 1 and Bus 2, works as the uncontrolled line. The voltage in the intermediate supply bus is distorted as the integration of all sources adds source voltage harmonics. Also, the loads to be connected across the load bus cannot be predicted and a significant contribution of nonlinear loads may exist, causing a high level of harmonic content in the current coming out of the intermediate supply bus.

The UPQC integrated in the uncontrolled distribution line imposes that the voltage at the load bus is harmonic-free. It also acts on the total load current, to compensate for current harmonics and reactive power, in a way that the total current coming out of the intermediate supply bus is also harmonic-free and in phase with the fundamental source voltage, resulting in unity power factor.

The inclusion of UPLC and UPQC in the system ensures that the harmonics level in the system is low. Besides, the control of reactive power in the high-frequency lines is achieved by those active filters. The reactive power flow in the controlled distribution line is obtained by the UPLC, whereas the UPQC ensures that the reactive power remains in the system and is compensated at the load bus so that the current coming out of the intermediate supply bus is in phase with the voltage.

For both UPQC and UPLC, the compensating reference current and voltage are calculated using the p-q theory, which was first proposed for three-phase system by Akagi *et al.* [6] and later adapted for the single-phase system [22], [23]. The p-q theory is advantageous in active filtering as it does not need calculation of root mean square (RMS) values or fast Fourier transform (FFT), which require a large computational time and affect the control system dynamics [6]. The basic equation behind all p-q theory-based active filters is given below

$$\begin{bmatrix} p \\ q \end{bmatrix} = \begin{bmatrix} V'_\alpha & V'_\beta \\ -V'_\beta & V'_\alpha \end{bmatrix} \cdot \begin{bmatrix} i_\alpha \\ i_\beta \end{bmatrix} = \begin{bmatrix} \bar{p} \\ \bar{q} \end{bmatrix} + \begin{bmatrix} \tilde{p} \\ \tilde{q} \end{bmatrix}. \quad (9)$$

The symbols $\bar{p}$, $\bar{q}$ denote the fundamental powers, whereas $\tilde{p}, \tilde{q}$ denote the harmonic powers. The α-β components of the voltage and currents are to be calculated first for implementing (9). The detailed description of the UPLC and UPQC operation can be found in [4]. After obtaining power components by (9), the controller calculates the compensating reference current and voltage, which are then synthesized using voltage-source PWM inverters [4]. It is also important to highlight that the PWM inverters, for both UPQC and UPLC, do not need any active voltage source, but only one capacitor each across their respective DC common buses.

IV. Distributed Intelligent Energy Management System

The proposed HFAC Microgrid system requires well-coordinated layers of control distributed throughout the system. The hierarchal levels exchange information among themselves in an iterative mode and as the level increases, the time horizon increases, i.e., lower level components or modules are usually faster than their higher level counterparts [14]. The HFAC Microgrid system has lower level microsource controllers associated with each energy source. Communications among microsources are not necessary for basic operation since each inverter is able to respond to load changes in a predetermined manner without communication of data from other sources or locations. The local lower level controllers for the UPLC and UPQC should also work faster.

The proposed DIEMS allows instantaneous optimization of alternative and renewable power sources. The use of storage requires an optimization scheme that considers the time-integral part of the load flow. So, the energy management has to perform energy scheduling a single day or multiple days ahead. An intelligent energy management system is thus required which enables short-term energy allocation scheduling at minimum costs based on power generation and load demand [7].

The function of the DIEMS is to generate set points for all the sources and storages in such a way that economically optimized power dispatch will be maintained to fulfill certain load demand. Generation forecast as well as some fast online algorithms are used to define the energy availability and, finally, to define the optimized power dispatch signals to the loads, as well as to the grid using the UPLC. This energy management system, consists of prediction module, optimization module, and online control module, is shown in the left-hand side of Fig. 4.

A. Prediction Module: Fuzzy ARTMAP

The predictions of generation is a complicated task for the Microgrid system because the sources connected are mainly the renewable energy sources where the capacity of generation varies largely with the external conditions like sunshine, temperature, etc. However, on the other hand, designing an efficient controller needs prediction of the generation with considerable accuracy [7]. Forecast of generation is not a very old topic and its relevance increases rapidly with more penetration of renewable energy sources in the power grid. In the proposed DIEMS, a Fuzzy ARTMAP-based day-type forecasting is used mainly with consideration of photovoltaic energy source, but it can be easily extended for use with other renewable-based energy sources. Knowledge of available future generation from renewable sources lets the DIEMS to store energy in advance, giving the system more flexibility to take advantage of real-time grid pricing by avoiding purchases or making a well-timed sale.

The basic ARTMAP is a class of NN architectures that perform incremental supervised learning of recognition categories and multidimensional maps in response to input vectors presented in an arbitrary order [10]. Fuzzy ARTMAP is a more general system that learns to classify inputs by a fuzzy set of

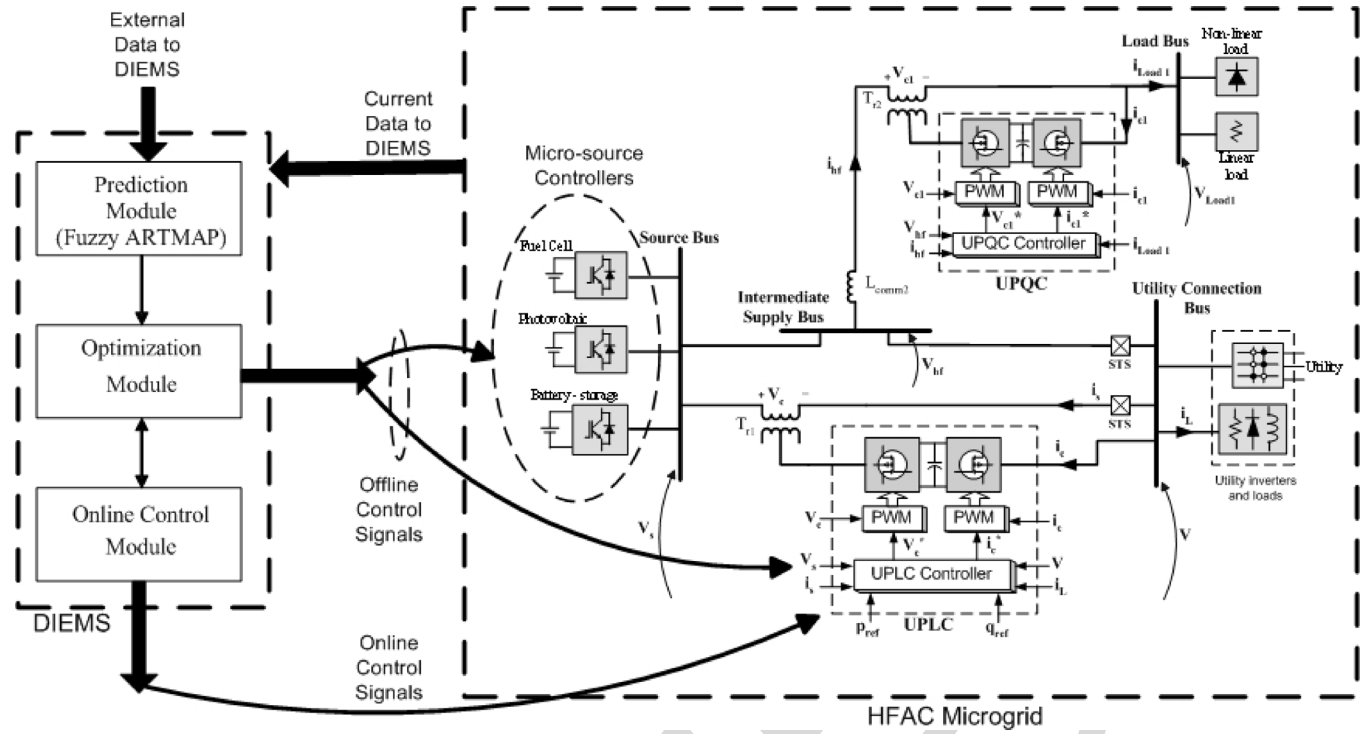

Fig. 4. Single-phase HFAC microgrid with active filters and DIEMS.

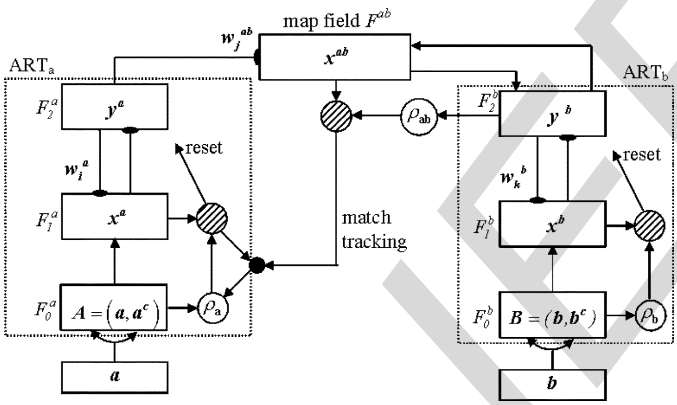

Fig. 5. Fuzzy ARTMAP structure.

features, or a pattern of fuzzy membership values between 0 and 1 indicating the extent to which each feature is present [11]. This generalization is accomplished by replacing ART1 modules of the binary ARTMAP system with fuzzy ART modules [11], [12]. Where ART1 dynamics are described in terms of set-theory operations, fuzzy ART dynamics are described in terms of fuzzy set theory operations. Thus, crisp intersection operators $(\cap, \cup)$ are replaced, respectively, by the fuzzy AND, OR operators $(\wedge, \vee)$ of the fuzzy set theory.

Each Fuzzy ARTMAP system includes a pair of Fuzzy ART modules ($\mathrm{ART_a}$ and $\mathrm{ART_b}$), as in Fig. 5, connected by an inter-ART module known as map field. During supervised learning, $\mathrm{ART_a}$ receives a stream $\{a^{(p)}\}$ of input patterns, and $\mathrm{ART_b}$ receives a stream $\{b^{(p)}\}$ of input patterns, where $b^{(p)}$ is the correct prediction given $a^{(p)}$. The map filed works as an associative learning network as well as an internal controller that ensures autonomous system operation in real time. The controller is designed to create the minimal number of $\mathrm{ART_a}$ recognition categories needed to meet accuracy criteria. The accuracy criteria is met by a min–max learning rule that enables a Fuzzy ARTMAP system to learn quickly, efficiently, and accurately as it conjointly minimizes predictive error and maximizes predictive generalization [11].

In this scheme, predictive success is automatically linked to category size on a trial-by-trial basis using only local operations. To do this, it increases the vigilance parameter ρ_a of $\mathrm{ART_a}$ by the minimal amount needed to correct a predictive error at $\mathrm{ART_b}$. Parameter ρ_a calibrates the minimum confidence that $\mathrm{ART_a}$ must have in a recognition category activated by an input $a^{(p)}$, in order to accept the category, rather than to search for a better one through an automatically controlled process of hypothesis testing. As in Fuzzy ART, lower ρ_a values lead to broader generalization and higher code compression. A predictive failure at $\mathrm{ART_b}$ increases ρ_a by the minimum amount needed to trigger hypothesis testing at $\mathrm{ART_a}$, using a mechanism called match tracking. Hypothesis testing leads to the selection of a new $\mathrm{ART_a}$ category which focuses attention on a new cluster of $a^{(p)}$ input features that is able to predict $b^{(p)}$ better. The details of Fuzzy ART learning rules can be found in [9] and [11]. The central concept of Fuzzy ARTMAP algorithm is the interaction between two Fuzzy ART mediated by the map field. The function of map field, as shown in Fig. 5, is described next based on [11] and [12].

1) $\mathrm{ART_a}$ *and* $\mathrm{ART_b}$*:* Inputs to the $\mathrm{ART_a}$ and $\mathrm{ART_b}$ are in the complement code form; for $\mathrm{ART_a}$, $\boldsymbol{I} = \boldsymbol{A} = (\boldsymbol{a}, \boldsymbol{a^c})$ and for $\mathrm{ART_b}$, $\boldsymbol{I} = \boldsymbol{B} = (\boldsymbol{b}, \boldsymbol{b^c})$. For $\mathrm{ART_a}$, $\boldsymbol{x^a} \equiv (x_1^a, \ldots, x_{2M_a}^a)$ denote the F_1^a output vector; $\boldsymbol{y^a} \equiv (y_1^a, \ldots, y_{N_a}^a)$ denote the F_2^a output vector; and $\boldsymbol{w_j^a} \equiv (w_{j1}^a, w_{j2}^a, \ldots, w_{j,2M_a}^a)$ denote

weight vector for j^{th} $\mathrm{ART_a}$. For $\mathrm{ART_b}$, $\boldsymbol{x^b} \equiv (x_1^b, \ldots, x_{2M_b}^b)$ denote the F_1^b output vector; $\boldsymbol{y^b} \equiv (y_1^b, \ldots, y_{N_b}^b)$ denote the F_2^b output vector; and $\boldsymbol{w_k^b} \equiv (w_{k1}^b, w_{k2}^b, \ldots, w_{k,2M_b}^b)$ denote the k^{th} $\mathrm{ART_b}$ weight vector. For the map field, $\boldsymbol{x^{ab}} \equiv (x_1^{ab}, \ldots, x_{N_b}^{ab})$ denote the F^{ab} output vector, and $\boldsymbol{w_j^{ab}} \equiv (w_{j1}^{ab}, w_{j2}^{ab}, \ldots, w_{j,N_b}^{ab})$ denote the weight vector from j^{th} F_2^a node to F^{ab}. Vectors $\boldsymbol{x^a}$, $\boldsymbol{y^a}$, $\boldsymbol{x^b}$, $\boldsymbol{y^b}$, and $\boldsymbol{x^{ab}}$ are set to $\mathbf{0}$ between input presentations.

2) Map Field Activation: One of the active $\mathrm{ART_a}$ or $\mathrm{ART_b}$ categories activates map field F^{ab}. If node J of F_2^a is chosen, then its weights $\boldsymbol{w_J^{ab}}$ activate F^{ab}. If node K in F_2^b is active, then the node K in F^{ab} is activated by 1-to-1 pathways between F_2^b and F^{ab}. If both $\mathrm{ART_a}$ and $\mathrm{ART_b}$ are active, then F^{ab} becomes active only if $\mathrm{ART_a}$ predicts the same category as $\mathrm{ART_b}$ via the weights $\boldsymbol{w_j^{ab}}$. The F^{ab} output vector $\boldsymbol{x^{ab}}$ is shown in (10) at the bottom of the page. By (10), $\boldsymbol{x^{ab}} = \mathbf{0}$ if the prediction $\boldsymbol{w_J^{ab}}$ is disconfirmed by $\boldsymbol{y^b}$. Such a mismatch event triggers an $\mathrm{ART_a}$ search for a better category, using match tracking as given next.

3) Match Tracking: At the start of each input presentation the $\mathrm{ART_a}$ vigilance parameter ρ_a equals to the baseline vigilance $\overline{\rho}_\mathrm{a}$. The map field vigilance parameter is ρ_{ab}. If

$$\left|\boldsymbol{x^{ab}}\right| < \rho_{\boldsymbol{ab}} \left|\boldsymbol{y^b}\right| \tag{11}$$

then ρ_a is increased until it is slightly larger than $\left|\boldsymbol{A} \wedge \boldsymbol{w_J^a}\right| |\boldsymbol{A}|^{-1}$, where $\boldsymbol{A}$ is the input to F_1^a, in complement coding form. Then

$$\left|\boldsymbol{x^a}\right| = \left|\boldsymbol{A} \wedge \boldsymbol{w_J^a}\right| < \rho_{\boldsymbol{a}} |\boldsymbol{A}| \tag{12}$$

where J is the index of the active F_2^a node. When this occurs, $\mathrm{ART_a}$ search leads either to activation of another F_2^a node J with

$$\left|\boldsymbol{x^a}\right| = \left|\boldsymbol{A} \wedge \boldsymbol{w_J^a}\right| \geq \rho_{\boldsymbol{a}} |\boldsymbol{A}| \tag{13}$$

$$\left|\boldsymbol{x^{ab}}\right| = \left|\boldsymbol{y^b} \wedge \boldsymbol{w_J^{ab}}\right| \geq \rho_{\boldsymbol{ab}} \left|\boldsymbol{y^b}\right| \tag{14}$$

or, if no such node exists, to the shutdown of F_2^a for the remainder of the input presentation.

4) Map Field Learning: Learning rules determine how the map field weights w_{jk}^{ab} change through time, as follows. Weights w_{jk}^{ab} in $F_2^a \rightarrow F^{ab}$ paths initially satisfy

$$w_{jk}^{ab}(0) = 1. \tag{15}$$

During resonance with the $\mathrm{ART_a}$ category J active, $\boldsymbol{w_J^{ab}}$ approaches the map field vector $\boldsymbol{x^{ab}}$. With fast learning, once J learns to predict the $\mathrm{ART_b}$ category K, that association is permanent; $w_{JK}^{ab} = 1$ for all time.

TABLE I
DATA USED FOR FUZZY ARTMAP TRAINING

Time (hour)	Temperature (°F)	Pressure (inch Hg)	R.H. (%)	Insolation (W/m²)
1253	73	24.59	19	977.10
1353	74	24.57	17	716.74
1453	75	24.57	18	567.35

TABLE II
OUTPUT CLASSIFICATION FOR DAY-TYPE PREDICTION

Insolation Quotient (InQ)	Output
0.8 – 1.0	1
0.6 – 0.8	2
0.4 – 0.6	3
0.25 – 0.4	4
0.1 – 0.25	5
< 0.1	6
Night	0

For hourly day-type forecasting, the weather inputs used in the Fuzzy ARTMAP are time, temperature, pressure, relative humidity (R.H.), and solar radiation (insolation) of Denver, CO, as shown partially in Table I.

The output day-type is classified based on the insolation quotient (InQ). This quotient can be calculated by dividing the hourly day time insolation data of a particular month with the corresponding hourly insolation data of the perfectly clear day in that month. The output classes are shown in Table II.

The day-type output is generally not available in the weather database. Only way to get the day-type is to consider the sky condition data. It is much easier to define the day-type based on Table II and those classes match well with the sky conditions data. Mainly considering the photovoltaic in the system, this day-type outputs help the DIEMS to know the amount of generation available from PV so that the DIEMS can store energy in advance of anticipated energy shortages. The same concept of day-type forecasting can be extended for wind forecasts for a wind energy-based system where more weather parameters are required as the inputs.

B. Optimization Module: Linear Programming

The goal of the optimization module is to optimize energy flows among generation, supply, and points of use to minimize operating cost or maximize profit in systems with DG. The output of this module is a set of recommended energy flows for a given period as a set of vectors from source to destination over each hour. The system can use available storage to offset expensive energy purchases or to store energy for an anticipated price

$$\boldsymbol{x^{ab}} = \begin{cases} \boldsymbol{y^b} \wedge \boldsymbol{w_J^{ab}}, & \text{if the } J\text{th } F_2^a \text{ node is active and } F_2^b \text{ is active} \\ \boldsymbol{w_J^{ab}}, & \text{if the } J\text{th } F_2^a \text{ node is active and } F_2^b \text{ is inactive} \\ \boldsymbol{y^b}, & \text{if } F_2^a \text{ is inactive and } F_2^b \text{ is active} \\ 0, & \text{if } F_2^a \text{ is inactive and } F_2^b \text{ is inactive} \end{cases} \tag{10}$$

TABLE III
OPERATING COST AND MAXIMUM AVAILABILITY OF DIFFERENT SOURCES

Sources	Operating Cost ($/kWh)	Maximum Availability (kW)
PV	0.005	1.0
Wind	0.07	0.1
Utility (buy)	0.09	2.0
Utility (sell)	0.03	2.0

spike. The optimization module minimizes the cost function for the system. The fixed costs are not considered because they are not influenced by the power dispatch. The goal function is made up by using; cost of generation by nonrenewable sources, cost associated grid and penalty cost. Violating boundary conditions such as underutilization of a unit causes the penalty costs.

In the HFAC Microgrid, renewable energy sources such as photovoltaic and wind energy are connected along with a 2 kWh lead-acid battery storage. The power can be send back to the utility only at the avoided cost as net metering is not available. The cost of operation and the maximum available power for each of the components are given below in Table III. The utility pricing data is obtained from [24].

The penalty costs are assumed \$0.20/kWh and \$0.10/kWh for the unused available solar and wind energy, respectively. These numbers are obtained based on the proportionate fixed costs of solar and wind power generation, as the unused available power implies more time to recover the fixed costs. Therefore, the fixed costs, though not used directly for optimization of power dispatch, will affect the cost equation in form of the penalty costs.

Based on this cost and availability structure, the goal function that is to be minimized can be formulated as follows:

$$C_k = G_{1,k}\cdot(0.005)+G_{2,k}\cdot(0.07)+GP_k\cdot(0.09)-GS_k\cdot(0.03) +(G_{1,k}^{\mathrm{Max}} - G_{1,k})\cdot(0.20)+(0.1-G_{2,k})\cdot(0.10) \quad (16)$$

where C_k is the total cost in \$ incurred during the kth hour; $G_{1,k}$ and $G_{2,k}$ are power generated in kW during the kth hour by the solar and wind sources, respectively; GP_k and GS_k are power in kW bought and sold from/to the utility, respectively, during kth hour; and $G_{1,k}^{\mathrm{Max}}$ is the maximum power available by the solar cell depending on the insolation available at kth hour.

The optimization module minimizes (16) such that the following constraints are obeyed:

$$S_{k+1} = S_k + \eta\cdot(G_{1,k}+G_{2,k}+GP_k-GS_k-L_k) \quad (17)$$
$$0 \le S_k \le 2.0 \quad (18)$$
$$0 \le G_{1,k} \le G_{1,k}^{\mathrm{Max}} \quad (19)$$
$$0 \le G_{2,k} \le 0.1 \quad (20)$$
$$0 \le GP_k \le 2.0 \quad (21)$$
$$0 \le GS_k \le 2.0 \quad (22)$$

where S_k and S_{k+1} are the storage state-of-charge at hour k and $k+1$; L_k is the load demand for kth hour; and η is the storage efficiency.

Equations (16)–(22) cannot be directly solved by linear programming because constraint (17) cannot be written in the general form $A.\vec{x} = \vec{b}$, where $\vec{b}$ must be a vector of constants [25]. Besides, for optimum operation, the storage should maintain a certain state-of-charge depending on the day-type. To overcome these problems, the knowledge of the storage dependence on day-type is incorporated into the optimization module. This heuristic-based optimization design is considered on the simple understanding that the charging and discharging patterns must be different if the system knows *a priori* the day-type for the present day and the next day. If the next day is going to be cloudy and the present day's generation is good, the DIEMS should be able to store more energy during the present day. This additional storage may increase present day's operation cost, but the savings during the next day will be more such that there will be a net increase in the total savings during the two-day operation.

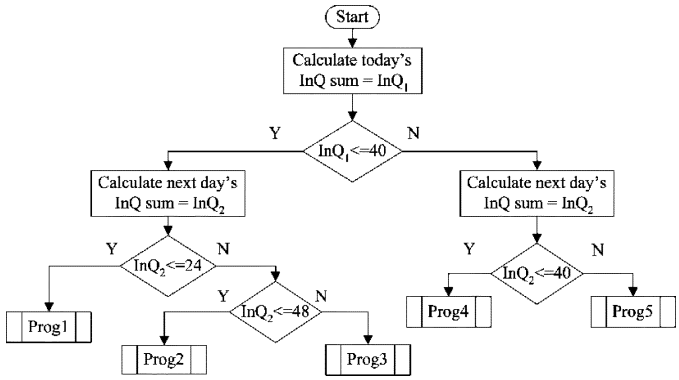

Fig. 6. Flowchart for selecting the optimization scheme.

In Fig. 6, the flowchart is given showing how an optimization scheme will be chosen. Based on present day's and next day's day-type forecasts (calculated in terms of Insolation Quotient or InQ), this program selects an optimization scheme out of five predefined schemes named as Prog1, Prog2, Prog3, Prog4, and Prog5. Each of these schemes are designed to have a particular end-of-day storage and different charging–discharging thresholds.

The flowchart for optimization scheme Prog2, when the present day is sunny and the next day is cloudy, is shown in Fig. 7. This flowchart is similar to all other schemes, where the main difference is the charging and discharging rates. In all of these schemes, the present day's future hours prediction information (InQ_{k+1}) is utilized, while defining the charging and discharging rates for the current hour, as shown in Fig. 7. After these rates are defined, linear programming is used to find the optimum power dispatch scheme.

For using the linear programming, constraint (17) is written in a different way.

Assuming AC–AC efficiency of the lead-acid battery is 80% and also assuming that charging efficiency and discharging efficiency are same

$$\eta_{\mathrm{charging}} = \eta_{\mathrm{discharging}} = 90\%. \quad (23)$$

Based on these assumptions, (17) can be rewritten in forms of the following two equations:

$$DS_{c,k} = (0.90)\cdot(G_{1,k}+G_{2,k}+GP_k-GS_k-L_k) \quad (24)$$
$$DS_{d,k} = \left(\frac{1}{0.90}\right)\cdot(L_k-G_{1,k}-G_{2,k}-GP_k+GS_k) \quad (25)$$

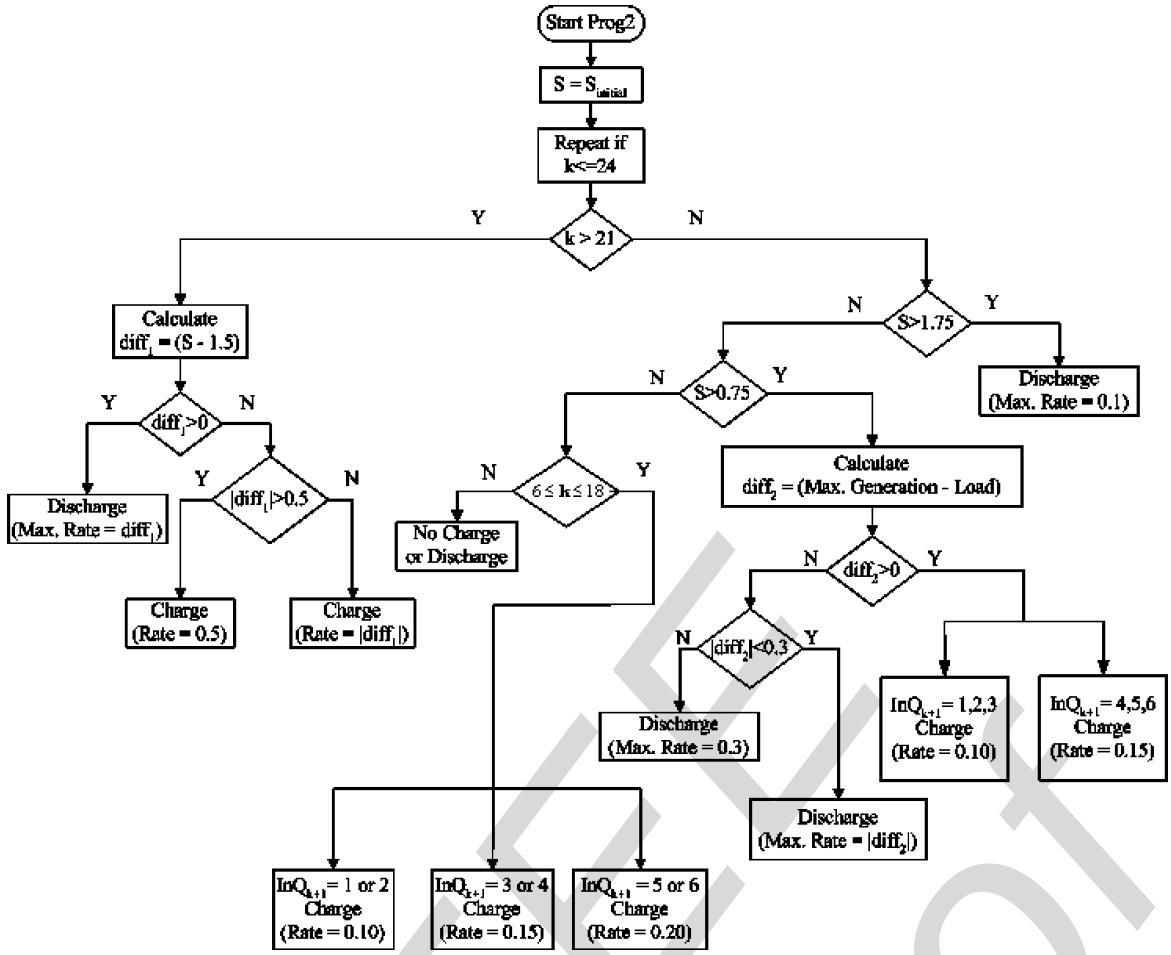

Fig. 7. Flowchart for optimization scheme Prog2.

where $DS_{c,k}$ is the amount of charging during kth hour and $DS_{d,k}$ is the discharge during kth hour. Due to the limitation on charging and discharge rate of the lead acid battery, (18) is also modified as

$$0 \leq DS_{c,k} \leq 0.5 \tag{26}$$

$$0 \leq DS_{d,k} \leq 0.5. \tag{27}$$

During charging in each optimization scheme, first the charging rate $DS_{c,k}$ is decided based on the heuristics given in the flowchart. Then, the linear programming is used to find optimum combination of $G_{1,k}$, $G_{2,k}$, GP_k, and GS_k. Similarly, during discharge, linear programming is used to find optimum $G_{1,k}$, $G_{2,k}$, GP_k, GS_k, and $DS_{d,k}$. In this case, the maximum discharge rate is decided based on the flowchart of the corresponding optimization scheme.

C. Online Control Module

The online control module, as shown in Fig. 4, operates the system in real-time. DIEMS generates the set points for the HFAC Microgrid based on the optimization module outputs. The measurements are fed back into the online control module where power balance is investigated. If actual conditions differ widely from the predicted ones because of the unexpected weather change for instance, this module deviates from the original optimization scheme and generates different set points for the UPLC. This in turn causes the change in the amount of power flow between the sources and the grid so that the power imbalance is avoided.

V. Simulation Results

The results showing the operation of single-phase HFAC Microgrid is discussed in this section. The first subsection shows the results corresponding to the HFAC Microgrid power flow and power quality control by the active filters. The training and testing results for the Fuzzy ARTMAP-based day-type forecasting are shown in the next section. Finally, in the last section, the results of cost optimization by the DIEMS optimization module are given.

A. HFAC Microgrid With Active Filters

Several simulations were done to evaluate the proposed single-phase HFAC Microgrid using the software PSIM™. A high-frequency voltage of amplitude 330 V and frequency 500 Hz with a 10% third-harmonic content is considered. The utility grid and inverter are represented by parallel association of a perfect voltage source of amplitude 330 V, 500 Hz, and loads constituting a diode bridge, 10 mH inductance, 100 Ω resistance, and 100 μF capacitance. In the load bus, a parallel association of highly inductive nonlinear loads (composed of

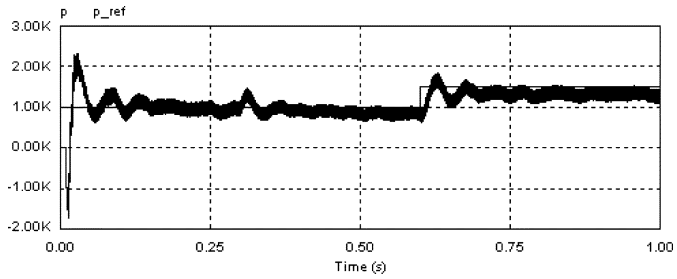

Fig. 8. Active power flow in the controlled distribution line.

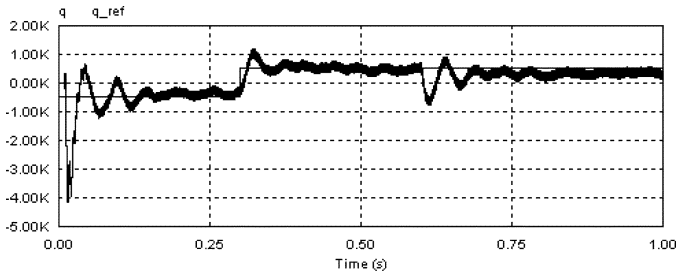

Fig. 9. Reactive power flow in the controlled distribution line.

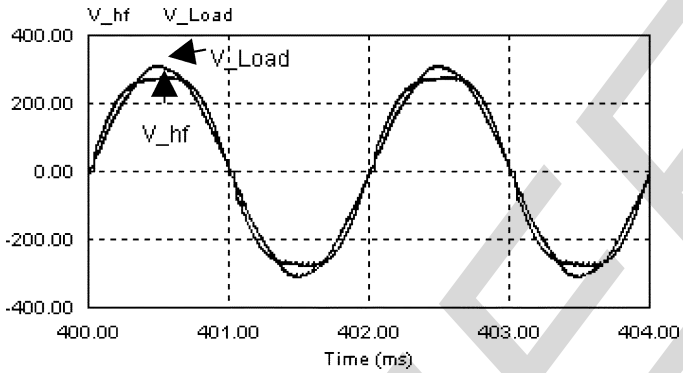

Fig. 10. Voltage before (V_hf) and after (V_Load) compensation.

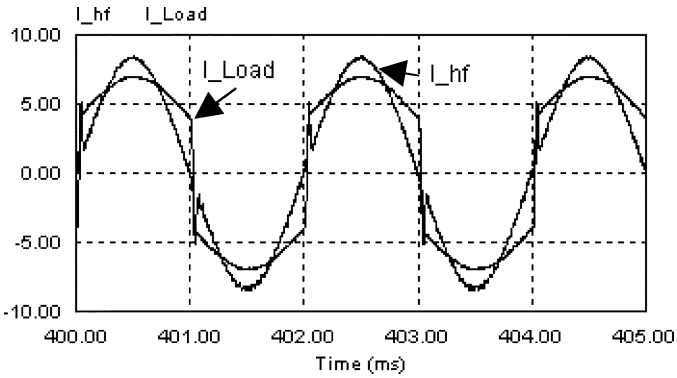

Fig. 11. Current before (I_Load) and after (I_hf) compensation.

TABLE IV
RESULTS OF TESTING AND TRAINING OF FUZZY ARTMAP

Input Data Used for Training	Testing Performance (% success)
Only Weather Inputs	66.8 %
Weather inputs and one previous hour output	68.4 %
Weather inputs and two previous hour outputs	71.9 %

TABLE V
RESULTS FROM CASE STUDY 2

	Data Used for Testing	Testing Performance (% success)
Before Training with September Data	January	100 %
	March	97.7 %
	June	100 %
	September	78.4 %
After Training with September Data	January	97.2 %
	March	95.6 %
	June	98.8 %
	September	100 %

a series connection of a diode bridge, a 50 Ω resistance, and a 1 H inductance), and a linear load (a 100 Ω resistance) are connected.

A step change in $q_{\rm ref}$ from −500–500 VAR is imposed at 0.3 s, while $p_{\rm ref}$ is constant at 1 kW. Then, $p_{\rm ref}$ is changed in step to 1.5 kW at 0.6 s. Here, $p_{\rm ref}$ and $q_{\rm ref}$ are the desired active and reactive power flow between source bus and grid through controlled distribution line.

It can be seen from Figs. 8 and 9, that the active and reactive power flow between the source bus and the utility connection bus are controlled by UPLC series active filter. The transient responses can be improved by optimizing the PI controllers in the UPLC series controller.

The voltage at intermediate supply bus (V_hf) has harmonics in it and the series active filter in the UPQC mitigates the source voltage harmonics, so the load voltage (V_Load) is harmonic free, as shown in Fig. 10. The harmonics in load current (I_Load), as in Fig. 11, is compensated by the shunt active filter in UPQC making the current from intermediate supply bus (I_hf) perfectly sinusoidal and in phase with the bus voltage. More detailed active filtering results for the single-phase HFAC Microgrid can be found in [4].

B. Fuzzy ARTMAP-Based Day-Type Prediction

The Fuzzy ARTMAP network is developed in C code and the hourly weather data for training and testing of this NN is collected from the National Climatic Data Center (NCDC) and National Renewable Energy Laboratory (NREL) websites [26], [27]. Some interesting case studies with the Fuzzy ARTMAP-based prediction are given next.

1) Case Study 1: The Fuzzy ARTMAP is trained with a single month's data and tested with a different month data. The inputs used, as shown in Table I, are the time, temperature, relative humidity, pressure, and insolation. All input data are scaled between 0 and 1 before using. As the length of the day varies with change in month, to compensate this effect, previous outputs are used as the additional inputs in some of the simulations. The results of the simulations are given in Table IV.

So, it can be concluded that using previous hour's output data as the inputs helps the NN to predict better.

TABLE VI
COST OF OPERATION FOR THE MICROGRID WITH AND WITHOUT DIEMS

	Day Type	Utility ($)	System ($)	Storage Reserve (kWh)	Number of Hours (<25% Charge)	Savings ($)	Savings (%)	Min. Storage (kWh)	DOD (%)
Without DIEMS	Sunny	$1.45	$0.84	0.10	6	$0.61	42.07%	0.10	95
	Cloudy	$1.23	$1.01	0.61	14	$0.22	17.89%	0.10	95
	Very Cloudy	$1.62	$1.50	0.36	1	$0.12	7.41%	0.36	82
	Very Cloudy	$1.62	$1.55	0.71	13	$0.07	4.32%	0.36	82
	Sunny	$1.45	$0.85	0.56	0	$0.60	41.38%	0.56	72
	Total	$7.37	$5.75		34	$1.62	21.98%		
With DIEMS	Sunny	$1.45	$0.82	1.50	0	$0.63	43.45%	0.50	75
	Cloudy	$1.23	$0.92	1.20	0	$0.31	25.20%	0.90	55
	Very Cloudy	$1.62	$1.52	1.20	0	$0.10	6.17%	0.89	55
	Very Cloudy	$1.62	$1.49	0.63	0	$0.13	8.02%	0.53	73
	Sunny	$1.45	$0.79	0.51	0	$0.66	45.52%	0.51	74
	Total	$7.37	$5.54		0	$1.83	24.83%		

2) Case Study 2: The Fuzzy ARTMAP is trained first with three months of data (January, March, and June) and tested with September data. Then, the previously trained NN is trained with September data and tested again.

From Table V, it is evident that Fuzzy ARTMAP can be trained with a new pattern without significant change in the previously trained system, the NN retains previously trained information, while continuing to learn new information. When the trained NN is tested with randomly chosen data from the four months database, it gave 99% success.

C. Cost Optimization

In the HFAC Microgrid, renewable energy sources such as photovoltaic and wind energy are connected along with a 2 kWh lead-acid battery storage. The power can be send back to the utility at the avoided cost. The cost of operation and the maximum available power for each of the components are already given in Table III.

For simulation, two systems are compared, one without the DIEMS and another with the DIEMS. A five-day window is considered where the consecutive days changes from sunny to cloudy then to very cloudy, then stays at very cloudy for the next day, and finally becomes sunny in the fifth day. The simulation results are shown in Table VI.

In Table VI, the utility column shows the cost of energy for a particular load profile if the Microgrid is absent. The system column gives the cost with the Microgrid system. Storage reserve indicates the end-of-day storage state-of-charge. Min. storage is the lowest state of charge attained by the battery during discharge. The maximum depth-of-discharge (DOD) for the storage in each day is shown in the final column.

It is evident that during the first sunny day, the increase in saving is small, only 1.38%, with DIEMS in operation. But in the next cloudy day, this saving increases to 7.31%. This is due to the fact that based on the day-type predictions, DIEMS knows that the future day is cloudy so it chooses an appropriate charge–discharge scheme. The increase of total cost savings for the five day window considered is about 3%. As both the cases without and with DIEMS relies on the same understanding of the charge–discharge of the storage, this small saving in the direct cost using DIEMS is significant considering the small system used here. Besides, the multifunctionality of the DIEMS helps to achieve indirect cost savings in the form of less maintenance and replacement cost which will be discussed later in this section. The avoided cost scenario only permits the user to sell the energy to the utility at wholesale cost which is significantly lower than the cost of buying energy from utility, for example, in the case studies, it is only 1/3 of the buying cost. The total savings using Microgrid-DIEMS during the five-day period is 24.83% which is significant considering that no real-time pricing or net metering is available. Though the simulated data are used in the cost optimization study, the data are compared with real-world data to make sure the validity of the work.

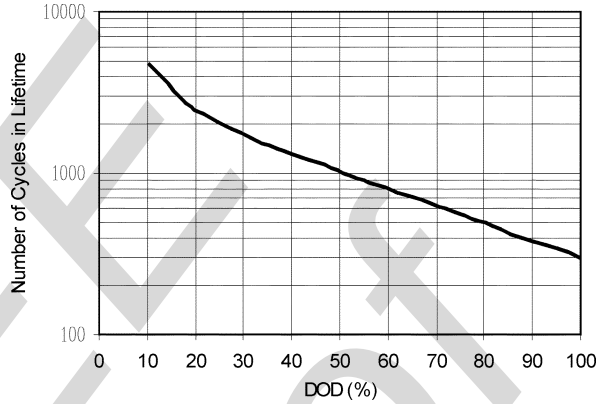

Fig. 12. Typical life expectancy curve of a lead-acid battery.

Another very important observation that can be made form Table VI is the number of hours when the storage state-of-charge is less than 25% of the full charge. The total number of hours for the system without DIEMS is 34 compared to zero such hours with DIEMS. The more such highly discharged hours, the more is the maintenance cost for storage.

Also, evident from Table VI is that the average DOD for the system without DIEMS is 85% compared to 66% with DIEMS. The DOD is defined as the amount of energy withdrawn from a battery or cell expressed as a percentage of its rated capacity. Now, as the DOD is related to the battery life, as shown in Fig. 12, at 66% average DOD, the number of cycles in lifetime is approximately 700; whereas at 85% of average DOD, it reduces to 421 cycles. If 200 charging and discharging cycles are assumed each year for the battery in the Microgrid, replacement

will be needed approximately in 3.5 years if the average DOD is 66%. But at 85% DOD, replacement will be needed in approximately in 2 years.

The cost of battery is generally expressed in $/kWh, where the levelized cost is used which includes the cost of battery as well as the operation and maintenance cost over the lifetime of the battery. For this paper, the replacement cost for the lead-acid battery is considered as $150/kWh, so that the total cost of replacement for the 2 kWh battery will be $300. Therefore, the extra cost of replacement due to higher average of DOD will be $64.3/year. This extra replacement cost combined with the additional maintenance cost can be thought as an average penalty cost of $0.15–$0.20/day to the system without DIEMS. Adding this penalty cost to the total operating cost without DIEMS from Table VI shows only 1% total savings during the five-day cycle when DIEMS is not used, compared with total savings of 24.83% for the system with DIEMS.

VI. Conclusion

In this paper, a single-phase HFAC Microgrid is shown as an exciting way to integrate renewable energy sources in a DG system. The adequate power flow and power quality control for the Microgrid is achieved by using single-phase p-q theory-based active filters, thus ensuring better utilization of the renewable sources. Also, shown in this paper that the cost of operation for this Microgrid can be optimized by implementing a DIEMS, consisting of a Fuzzy ARTMAP NN for prediction and an optimization module.

The simulation results showed that by using UPLC the active and reactive power flow can be controlled between the grid and the renewable sources. In addition, using UPQC makes the current from the intermediate supply bus approximately sinusoidal and in phase with the fundamental source voltage. Also, UPQC helps to compensate for voltage distortions, resulting in a sinusoidal load voltage. This is an important aspect when considering voltage sensitive loads connected to the systems, which can be adversely affected by poor voltage waveforms.

The results also showed that the Fuzzy ARTMAP was successfully able to predict hourly day-type based on the weather inputs. It is also evident that a Fuzzy ARTMAP structure can be trained with a new pattern without significant change in the previously trained system. This is important while forecasting a new day-type which can be significantly different than the training patterns.

Based on successful day-type forecasting, the cost optimization module for the DIEMS is developed using linear programming along with heuristics. The results obtained showed that this optimization module not only decreases the cost of operation, but also helps to improve overall system operation such as lower depth-of-discharge for the storage and improved battery life. The future scope of this work will concentrate efforts on developing dynamic programming-based optimization and implementing optimization module in the DIEMS using adaptive NN.

References

[1] R. H. Lasseter, "MicroGrids," in *Proc. PES Winter Meeting*, Jan. 27–31, 2002, vol. 1, pp. 305–308.

[2] A. Borbely and J. F. Kreider, *Distributed Generation: The Power Paradigm for the New Millennium*. Boca Raton, FL: CRC, 2001.

[3] H. Fujita and H. Akagi, "The unified power quality conditioner: The integration of series and shunt-active filters," *IEEE Trans. Power Electron.*, vol. 13, no. 2, pp. 315–322, Mar. 1998.

[4] S. Chakraborty and M. G. Simões, "Advanced active filtering in a single phase high frequency AC Microgrid," in *Proc. IEEE-Power Electron. Specialist Conf., PESC* , Recife, Brazil, Jun. 12–16, 2005, pp. 191–197.

[5] A. Aredes, K. Heumann, and E. H. Watanabe, "An universal active power line conditioner," *IEEE Trans. Power Del.*, vol. 12, no. 2, pp. 545–551, Apr. 1998.

[6] H. Akagi, Y. Kanazawa, and A. Nabae, "Generalized theory of the instantaneous reactive power in three-phase circuits," in *Proc. Int. Power Electron. Conf., IPEC*, Tokyo, Japan, 1983, pp. 1375–1386.

[7] ***[Kindly provide page numbers]*** G. Winkler, C. Meisenbach, M. Hable, and P. Meier, "Intelligent energy management of electrical power systems with distributed feeding on the basis of forecasts of demand and generation," in *Proc. 16th Int. Conf. Exhib. Electricity Distrib., CIRED*, Jun. 2001, Conference publication No. 482, 4.31, IEE 2001.

[8] G. A. Carpenter and S. Grossberg, "A massively parallel architecture for a self-organizing neural pattern recognition machine," *Comput., Vision, Graphics, Image Process.*, vol. 37, pp. 54–115, 1987.

[9] G. A. Carpenter, S. Grossberg, and D. B. Rosen, "Fuzzy ART: Fast stable learning and categorization of analog patterns by an adaptive resonance system," *Neural Netw.*, vol. 4, no. 6, pp. 759–771, 1991.

[10] G. A. Carpenter, S. Grossberg, and J. H. Reynolds, "ARTMAP: Supervised real-time learning and classification of nonstationary data by a self-organizing neural network," *Neural Netw.*, vol. 4, no. 5, pp. 565–588, 1991.

[11] G. A. Carpenter, S. Grossberg, N. Markuzon, and J. H. Reynolds, "Fuzzy ARTMAP: A neural network architecture for incremental supervised learning of analog multidimensional maps," *IEEE Trans. Neural Netw.*, vol. 3, no. 5, pp. 698–713, 1992.

[12] ***[Kindly provide publisher/location]*** G. A. Carpenter and S. Grossberg, "Self-organizing neural networks for supervised and unsupervised learning and prediction," in *From Statistics to Neural Networks*, ser. NATO ASI Series, V. Cherkassky, J. H. Friedman, and H. Wechsler, Eds. : , 1994.

[13] P. K. Sood and T. A. Lipo, "Power conversion distribution system using a high-frequency ac link," *IEEE Trans. Ind. Appl.*, vol. 24, no. 2, pp. 288–300, Mar./Apr. 1998.

[14] M. G. Simões, S. Chakraborty, F. A. Farret, and J. M. Corrêa, "Intelligent based hierarchical control of power electronics for distributed generation systems," in *Proc. Workshop Power Electron. Fuel Cells, National Fuel Cell Research Center*, Irvine, CA, Aug. 8–9, 2002.

[15] S. A. Nasar and F. C. Trutt, *Electric Power Systems*. Boca Raton, FL: CRC, 1999.

[16] B. Gustavsen, J. A. Martinez, and D. Durbak, "Parameter determination for modeling system transients-Part II: Insulated cables," *IEEE Trans. Power Del.*, vol. 20, no. 3, pp. 2045–2050, Jul. 2005.

[17] N. Amekawa, N. Nagaoka, and A. Ametani, "Impedance derivation and wave propagation characteristics of pipe-enclosed and tunnel-installed cables," *IEEE Trans. Power Del.*, vol. 19, no. 1, pp. 380–386, Jan. 2004.

[18] L. Zhou and S. A. Boggs, "High frequency attenuating cable for protection of low-voltage AC motors fed by PWM inverters," *IEEE Trans. Power Del.*, vol. 20, no. 2, pp. 548–553, Apr. 2005.

[19] U. Borup, B. V. Nielsen, and F. Blaabjerg, "Compensation of cable voltage drops and automatic identification of cable parameters in 400 Hz ground power units," *IEEE Trans. Ind. Appl.*, vol. 40, no. 5, pp. 1281–1286, Sep./Oct. 2004.

[20] I. Takahashi and G. J. Su, "A 500 Hz power system-applications," in *Proc. IEEE–IAS Annu. Meeting Conf. Rec.*, Oct. 1–5, 1989, vol. 1, pp. 996–1002.

[21] ——, "A 500 Hz power system-power converter and transmission lines," in *Proc. IEEE–IAS Annu. Meeting Conf. Rec.*, Oct. 1–5, 1989, vol. 1, pp. 988–995.

[22] J. M. Corrêa, S. Chakraborty, M. G. Simões, and F. A. Farret, "A single phase high frequency AC Microgrid with an unified power quality conditioner," in *Proc. IEEE 38th–IAS Annu. Meeting Conf. Rec.*, Salt Lake City, UT, Oct. 2003, vol. 2, pp. 956–962.

[23] J. Liu, J. Yang, and Z. Wang, "A new approach for single-phase harmonic current detecting and its application in a hybrid active power filter," in *Proc. 25th Annu. Conf. IEEE Ind. Electron. Soc.–IECON*, Nov. – Dec. 29 – 3, 1999, vol. 2, pp. 849–854.

[24] Electric Tariff Index, Public Service Company of Colorado, 1996.

[25] S. I. Gass, *Linear Programming: Methods and Applications*. Boston, MA: Boyd & Fraser, 1995.
[26] Unedited Local Climatological Data, National Climatic Data Center (NCDC). [Online]. Available: www.ncdc.noaa.gov/servlets/ULCD
[27] Measurement and Instrumentation Data Center (MIDC), National Renewable Energy Laboratory (NREL). [Online]. Available: http://www.nrel.gov/midc/

Sudipta Chakraborty (S'02) was born in Kolkata, India, in 1979. He received the B.E. degree in electrical engineering from Bengal Engineering College (now Bengal Engineering and Science University), Bengal, India, in 2001. He is currently working towards the Ph.D. degree in engineering systems, electrical specialty at the Colorado School of Mines, Golden.

He is currently working on intelligent integration of renewable sources in the Microgrid so that the power quality and power flow issues can be resolved. Before coming to U.S., he worked for a short-term in an AICTE funded project on advanced drives system as a Research Assistant. His research interests include renewable energy, control systems, power electronics, intelligent control, and power systems.

Mr. Chakraborty was the recipient of several awards and scholarships from the Government of India for his scholastic achievements. He received the Myron Zuker Travel Grant from IEEE to attend 38th Annual Meeting of the IEEE Industrial Applications Society held in Salt Lake City, UT, in 2003. Recently, he was awarded with the IEEE Industrial Electronics Society Scholarship to attend and present his paper at IECON 2005, Raleigh, NC.

Manoja D. Weiss (S'92–M'01) received the B.S.E.E. degree from Grove City College, Grove City, PA, in 1993, the M.S.E.E. degree from the Pennsylvania State University, University Park, in 1995, and the Ph.D. degree in electrical engineering from the University of Colorado, Boulder, in 2001. Her Ph.D. research was on microwave high-efficiency power amplifiers.

From 2001 to 2003, she worked at Phiar Coorporation, Boulder, CO, as an Electromagnetics Engineer, designing and building nanoscale antenna-coupled diode detectors for operation in the Terahertz range. She joined the faculty of the Colorado School of Mines, Golden, in 2003, and is working towards establishing a program of research and education in RF/microwave and wireless systems.

M. Godoy Simões (S'89–M'95–SM'98) received the B.S. and M.Sc. degrees in electrical engineering from the University of São Paulo, São Paulo, Brazil, in 1985 and 1990, respectively, the Ph.D. degree in electrical engineering from the University of Tennessee, Knoxville, in 1995, and the Livre-Docencia (D.Sc.) degree in mechanical engineering from the University of São Paulo, in 1998.

He joined the faculty of the Colorado School of Mines, Golden, in 2000, and has been working to establish research and education activities in the development of intelligent control for high-power electronics applications in renewable and distributed energy systems. He authored the book *Renewable Energy Systems: Design and Analysis With Induction Generators* (Boca Raton, FL: CRC), and *Integration of Alternative Sources of Energy*, (New York: Wiley)

Dr. Simões is a recipient of a National Science Foundation (NSF)–Faculty Early Career Development (CAREER) Award in 2002, the NSF's most prestigious award for new faculty members. He served as the Program Chair for the Power Electronics Specialists Conference 2005, as well as the General Chair of the Power Electronics Education Workshop 2005. He is serving as the Chair of the IEEE Power Electronics Chapter of the Denver Section, IEEE Power Electronics Society Intersociety Chairman, and also as the Associate-Editor for the IEEE TRANSACTIONS ON POWER ELECTRONICS.